

SCIENTIFIC REPORTS

OPEN

Enhanced magnetocaloric effect in Ni-Mn-Sn-Co alloys with two successive magnetostructural transformations

Xuexi Zhang , Hehe Zhang, Mingfang Qian & Lin Geng

High magnetocaloric refrigeration performance requires large magnetic entropy change ΔS_M and broad working temperature span ΔT_{FWHM} . A fourth element doping of Co in ternary Ni-Mn-Sn alloy may significantly enhance the saturation magnetization of the alloy and thus enhance the ΔS_M . Here, the effects of Co-doping on the martensite transformation, magnetic properties and magnetocaloric effects (MCE) of quaternary $\text{Ni}_{47-x}\text{Mn}_{43}\text{Sn}_{10}\text{Co}_x$ ($x = 0, 6, 11$) alloys were investigated. The martensite transformation temperatures decrease while austenite Curie point increases with Co content increasing to $x = 6$ and 11 , thus broadening the temperature window for a high magnetization austenite ($13.5, 91.7$ and $109.1 \text{ A}\cdot\text{m}^2/\text{kg}$ for $x = 0, 6$ and 11 , respectively). Two successive magnetostructural transformations ($A \rightarrow 10\text{M}$ and $A \rightarrow 10\text{M} + 6\text{M}$) occur in the alloy $x = 6$, which are responsible for the giant magnetic entropy change $\Delta S_M = 29.5 \text{ J/kg}\cdot\text{K}$, wide working temperature span $\Delta T_{FWHM} = 14 \text{ K}$ and large effective refrigeration capacity $RC_{eff} = 232 \text{ J/kg}$ under a magnetic field of 5.0T . These results suggest that $\text{Ni}_{40.6}\text{Mn}_{43.3}\text{Sn}_{10.0}\text{Co}_{6.1}$ alloy may act as a potential solid-state magnetic refrigerant working at room temperature.

Over the last decade, Ni-Mn-X ($X = \text{Sn, In and Sb}$) metamagnetic shape memory alloys (MSMAs) have attracted significant interests due to their potential applications as magnetic refrigeration materials near room temperature. These materials, based on magnetocaloric effect (MCE), are considered to be environmentally friendly and cost-effective refrigerants because of their large refrigeration capacity (RC) which is comparable to those of expensive rare-earth-containing MCE compounds¹. In Ni-Mn-X-based ($X = \text{Sn, In and Sb}$) alloys, the metamagnetic structural transition from the weak-magnetic martensite to ferromagnetic austenite under an applied magnetic field leads to an inverse MCE^{2–4}, whereas the magnetic transition of the austenite phase is responsible for a conventional MCE^{5–7}. Clearly, the metamagnetic transition is driven by the Zeeman energy $E_{zeeman} = \mu_0 H \Delta M$, where ΔM and $\mu_0 H$ represent the magnetization difference between martensite/austenite phases and the applied magnetic field, respectively. So, enhanced ΔM is in favor of large E_{zeeman} , which is responsible for the high magnetic entropy change (ΔS_M) and wide working temperature span (ΔT_{FWHM} , defined as the full width at half maximum of the magnetic entropy peak)⁸, where the ΔT_{FWHM} is crucial for magnetic refrigeration applications in the case of inverse MCE^{9,10}.

In Ni-Mn-X off-stoichiometric MSMAs, the ΔM can be enhanced by composition tuning^{11,12}, heat treatment^{13,14} and doping^{15,16}. It has been reported that high-Mn content Ni-Mn-X alloys exhibited enhanced ΔM because the magnetization of the austenite was mainly attributed to the ferromagnetic interaction between the neighboring Mn-Mn atoms¹⁷. For instance, the austenite of Mn-rich $\text{Ni}_{43}\text{Mn}_{46}\text{Sn}_{11}$ alloy¹⁸ shows a higher magnetization of $68 \text{ A}\cdot\text{m}^2/\text{kg}$ under a magnetic field of 5.0 T , compared to that of $39 \text{ A}\cdot\text{m}^2/\text{kg}$ for $\text{Ni}_{46}\text{Mn}_{43}\text{Sn}_{11}$ alloy¹⁹. Heat treatment is also a useful method to modulate the grain constraint in order to control the microstructure, martensite transformation (MT) temperature and magnetic properties of the ferromagnetic MSMAs (FMSMAs)^{20,21}. Doping of non-ferromagnetic elements^{22–24} such as Cu, Al and Ti can enhance ΔM effectively by tuning the valence electron concentration e/a or changing the unit cell volume, which mainly changes the MT temperatures. Of note is that the doping of ferromagnetic elements such as Fe and Co can effectively improve the ΔM . For instance, the substitution of Fe for Ni can simultaneously enhance the magnetic-field-induced reverse

School of Materials Science and Engineering, Harbin Institute of Technology, Harbin, 150001, China. Correspondence and requests for materials should be addressed to X.Z. (email: xxzhang@hit.edu.cn)

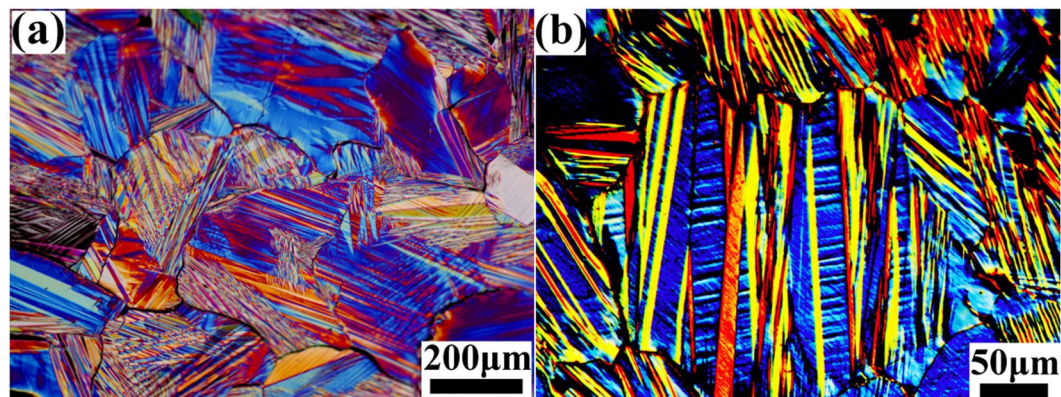


Figure 1. Optical microscope (OM) images showing the grains and martensite twin morphology in the Co6 alloy. (a) and (b) are low and high magnification images, respectively.

martensitic transformation and mechanical properties of Ni-Mn-Sn^{25–27}. Previous studies suggested that Co substitution for Ni in Ni-Mn-X alloys can effectively improve the austenite saturation magnetization and decrease the martensite magnetization^{28–30}, which was mainly due to the following four aspects: 1) The introduction of Co acted as a “ferromagnetic activator” to induce the magnetic moments of the nearest neighboring Mn-Mn atoms aligning in a ferromagnetic order^{31,32}, 2) Upon substitution of Co for Ni in Ni-Mn-X alloys, the austenite Curie point (T_C^A) increased significantly with increasing Co concentration, which broadened the temperature window of the high magnetization austenite³³, 3) The doping of Co can increase the Curie point and saturation magnetization of the Ni-Mn-X alloys, which accordingly increases the E_{zeeman} ³⁴, 4) Co atoms at Ni site contribute a much larger magnetic moment ($\sim 1.0 \mu_B$) compared to that of Ni ($\sim 0.3 \mu_B$) in the austenite³⁵.

The enlargement of ΔT_{FWHM} may be realized by two successive magnetostructural transformations, which have been found in some ferromagnetic alloys. For example, rare earth containing low temperature magnetic refrigeration compounds, such as TbMn₂Si₂³⁶, ErGa³⁷, DyB₂³⁸, HoPdIn³⁹, may exhibit a two successive magnetic transitions behavior deriving from the coupling of spin-reorientation temperature (TSR) and Curie temperature (T_C); Two successive ΔS_M peaks with the same sign, associated with a first-order martensite transformation (MT) and an intermediate martensite transformation (IMT), have also been discovered in some Ni-Mn-X alloys after composition tuning or under external pressure^{40–42}. These two adjacent transformations lead to a partially overlap of the refrigerant temperature intervals, yielding an improved refrigerating capacity. Here, we reported the MT, magnetic transition and MCE of Ni_{47-x}Mn₄₃Sn₁₀Co_x ($x = 0, 6, 11$) alloys. Two successive magnetostructural transformations from austenite phase to two different modulated martensite phases, i.e. $A \rightarrow 10M$ and $A \rightarrow 10M + 6M$, were demonstrated in the Ni_{40.6}Mn_{43.3}Sn_{10.0}Co_{6.1} (Co6) alloy induced by an external magnetic field. As a consequence, a large magnetic entropy change ΔS_M of 29.5 J/kg·K with a wide ΔT_{FWHM} of ~ 14 K attributed to the occurrence of successive magnetostructural transformations and a strong metamagnetic transition behavior were revealed in the Co6 alloy.

Results and Discussion

Microstructure of the Ni_{40.6}Mn_{43.3}Sn_{10.0}Co_{6.1} (Co6) alloy. The typical microstructure of the martensite phase of the Co6 alloy is shown in Fig. 1, where the sample was firstly kept in the ice water for several minutes to reach the martensite state. The microstructure is very similar to those modulated martensite structures reported in some ferromagnetic shape memory alloys⁴³. Many cracks distributed along the grain boundaries were observed, as shown in Fig. 1a, implying the brittleness of the polycrystalline alloy. In addition, the martensite morphology is plate-like, which can be recognized by the straight twin boundaries of each plate. Fine twins with thickness of 2–10 μm exist inside the broad martensite plates, as shown in Fig. 1b. Previous report⁴⁴ showed that different martensite structures possess different morphologies for Ni-Mn-Sn alloys, where the 10M martensite exhibited broad plate morphology, 14M martensite a fine form and the unmodulated structure ($L1_0$) in between. The co-existence of the martensite twins with different widths in the present work implied the existence of different martensite structures in Co6 alloy at room temperature (RT). Detailed martensite structure of the present alloy will be analyzed by XRD and discussed in the later sections.

Martensite transformation of Ni_{47-x}Mn₄₃Sn₁₀Co_x ($x = 0, 6, 11$) alloys. Figure 2 shows the DSC curves of Ni_{47-x}Mn₄₃Sn₁₀Co_x ($x = 0, 6, 11$) alloys in the temperature range 220–500 K. The strong exothermic and endothermic peaks produced by the forward and reverse MT correspond to the starting and finishing temperatures M_s^{DSC} , M_f^{DSC} , A_s^{DSC} and A_f^{DSC} , respectively, determined by the intersection of the base-line and tangent line. These temperatures are summarized in Table 1 together with the values of the valence electrons per atom (e/a). With the addition of Co element, a monotonic decrease in the MT temperatures occurs, as shown in Table 1. Generally, the change in MT temperatures can be interpreted from the following two aspects. Firstly, the e/a dependence of MT temperatures has been found to increase monotonically in Ni-Mn-based Heusler alloys^{45,46}. It has been supposed that the $L2_1$ austenite is stabilized because its Fermi surface just touches the Brillouin zone boundary⁴⁷. With e/a increasing and thus the Fermi surface overlapping the Brillouin zone, the

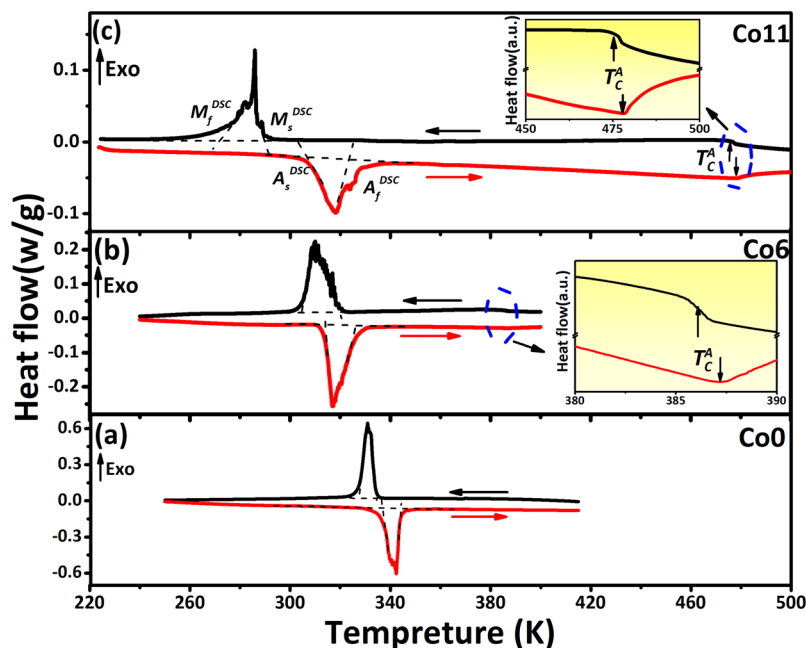


Figure 2. Differential scanning calorimetry (DSC) plots of the annealed $\text{Ni}_{47-x}\text{Mn}_{43}\text{Sn}_{10}\text{Co}_x$ ($x = 0, 6, 11$) alloys at heating and cooling rates of 10 K/min. (a) Co0, (b) Co6 and (c) Co11. Insets in (b) and (c) are enlarged images showing the magnetic transitions around the Curie point.

Alloys	Transformation temperatures, K					ΔH_{endo} , J/g	$\Delta S_{\text{tr}}^{\text{endo}}$, J/kg·K	ΔH_{exo} , J/g	$\Delta S_{\text{tr}}^{\text{exo}}$, J/kg·K
	A_s^{DSC}	A_f^{DSC}	M_s^{DSC}	M_f^{DSC}	T_C^A				
Co0 ^{1*}	336	344	334	327	—	16.5 ± 0.2	48.5 ± 0.5	16.9 ± 0.1	51.1 ± 0.3
Co6 ^{2*}	314	326	310	304	387	10.8 ± 0.06	33.7 ± 0.2	9.9 ± 0.06	32.2 ± 0.2
Co11 ^{3*}	307	323	289	271	476	5.5 ± 0.2	17.7 ± 0.6	4.7 ± 0.2	16.9 ± 0.6

Table 1. Martensite transformation temperatures (A_s^{DSC} , A_f^{DSC} , M_s^{DSC} , M_f^{DSC}), Curie point (T_C^A), transformation enthalpy change (ΔH_{endo} and ΔH_{exo}) and transformation entropy change ($\Delta S_{\text{tr}}^{\text{endo}}$ and $\Delta S_{\text{tr}}^{\text{exo}}$) during heating/cooling process obtained by DSC curves of $\text{Ni}_{47-x}\text{Mn}_{43}\text{Sn}_{10}\text{Co}_x$ ($x = 0, 6, 11$) alloys. ^{1*}Co0 - $\text{Ni}_{45.6 \pm 0.2}\text{Mn}_{43.6 \pm 0.1}\text{Sn}_{10.8 \pm 0.1}$, ^{2*}Co6 - $\text{Ni}_{40.6 \pm 0.1}\text{Mn}_{43.3 \pm 0.1}\text{Sn}_{10.0 \pm 0.04}\text{Co}_{6.1 \pm 0.04}$, ^{3*}Co11 - $\text{Ni}_{35.7 \pm 0.2}\text{Mn}_{44.1 \pm 0.2}\text{Sn}_{9.2 \pm 0.06}\text{Co}_{11.0 \pm 0.1}$ (data indicate atomic percent, at. %).

L_2 austenite structure becomes unstable, which induces the occurrence of the MT⁴⁷. Here, the values of e/a are the concentration-weighted sum of s , d , and p valence electrons, i.e. 10 ($3d^84s^2$) for Ni, 7 ($3d^54s^2$) for Mn, 4 ($5s^25p^2$) for Sn and 9 ($3d^74s^2$) for Co, respectively. The calculated e/a decreases with increasing Co substitution of Ni mainly because the valence electrons of Co is less than Ni, thus decreasing the MT temperatures of the alloy, which is in good agreement with the e/a dependence rule^{45,46}. On the other hand, the atom size effect, originating from the unit cell expansion of the austenite, is not favorable to the occurrence of MT due to changes of the relative positions between the Fermi surface and Brillouin zone²⁹. The substitution of larger Co atoms (atomic radius $r = 0.126$ nm) for smaller Ni atoms ($r = 0.125$ nm) causes a slight expansion of the austenitic unit cell. Both factors stabilize the austenite phase and therefore decrease the MT temperatures.

A further feature of weak shoulder thermal effect (T_C^A) is also observed for sample Co6 and Co11, as shown in the inset in Fig. 2b,c, respectively, which corresponds to the magnetic transition from ferromagnetism to paramagnetism of the austenite during cooling process. But the T_C^A point was not found for Co0 probably because the magnetic transition occurs below MT temperatures leading to the extremely low magnetization of the austenite (as shown in Fig. 3a). Therefore, it can be deduced that the substitution of Co for Ni in Ni-Mn-Sn alloys effectively increases the T_C^A , which is consistent with refs^{29,30}. The comparison of the transformation entropy changes during heating ($\Delta S_{\text{tr}}^{\text{endo}}$) and cooling ($\Delta S_{\text{tr}}^{\text{exo}}$) process are also listed in Table 1 ($\Delta S_{\text{tr}}^{\text{endo}} = \Delta H_{\text{endo}}/T_t$, where $T_t = (A_s^{\text{DSC}} + A_f^{\text{DSC}})/2$; $\Delta S_{\text{tr}}^{\text{exo}} = \Delta H_{\text{exo}}/T_p$, where $T_p = (M_s^{\text{DSC}} + M_f^{\text{DSC}})/2$). ΔH_{endo} and ΔH_{exo} denote as the enthalpy changes during the inverse and direct MT, was obtained from the area between the DSC peaks and the baseline. The results show that the difference between $\Delta S_{\text{tr}}^{\text{endo}}$ and $\Delta S_{\text{tr}}^{\text{exo}}$ are very small (≤ 2.6 J/kg·K).

Figure 3 shows the field-heating (FH) and field-cooling (FC) magnetization vs temperature plots (M - T) of $\text{Ni}_{47-x}\text{Mn}_{43}\text{Sn}_{10}\text{Co}_x$ ($x = 0, 6, 11$) alloys measured under magnetic fields of 0.02 and 5.0 T. The magnetization change (ΔM) in Co0 between austenite and martensite phases during MT is very small (Fig. 3a) because the phase transformation temperatures are higher than the magnetic transition point ($T_{\text{tr}} > T_C^A$) and thus MT occurs in a weak-magnetic state. Furthermore, the metamagnetic transition behavior is also weak in Co0 alloy, i.e. its MT

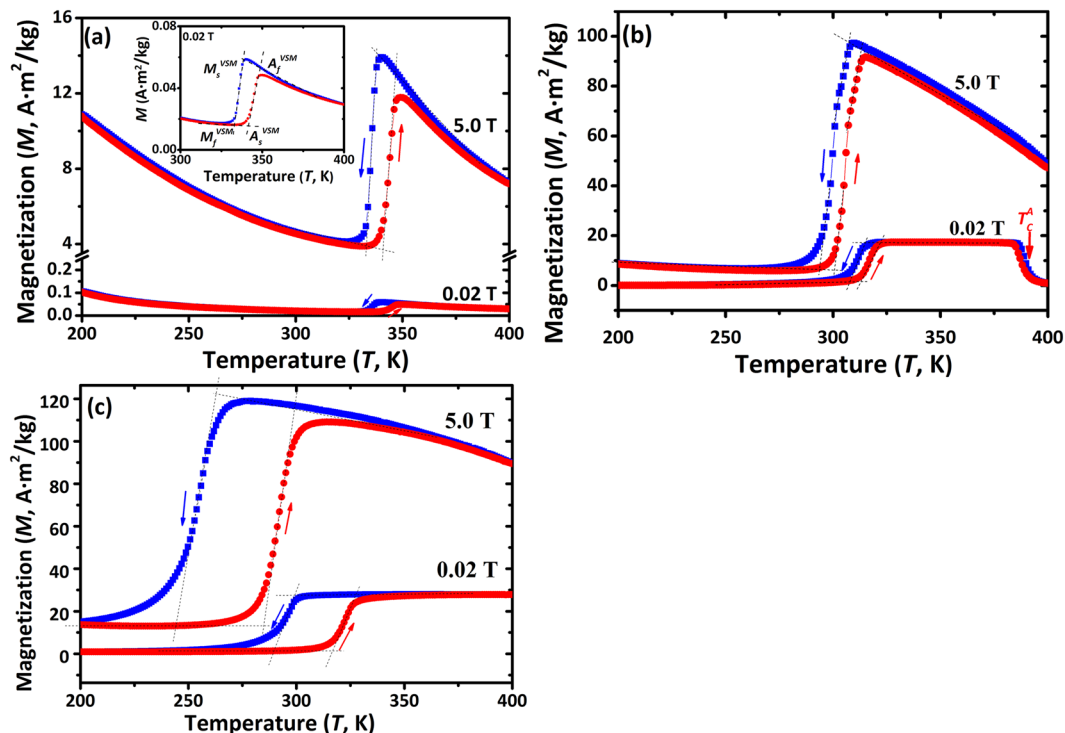


Figure 3. Temperature dependence of the magnetization (M - T) curves under external magnetic fields of 0.02 and 5.0 T for the alloys of (a) Co0, (b) Co6 and (c) Co11. The inset in (a) shows an enlarged M - T curves of Co0 alloy under a magnetic field of 0.02 T.

Alloys	Magnetic field, T	Transformation temperatures, K					ΔT_{Hys}^{1*}	Magnetization ^{2*} , A·m ² /kg			$\Delta A_s/\Delta H$, K/T
		A_s^{VSM}	A_f^{VSM}	M_s^{VSM}	M_f^{VSM}	M_M		M_A	ΔM^{3*}		
Co0	0.02	341	349	338	333	9.5	0.02	0.06	0.04	-0.2	
	5.0	340	348	338	332	9	4.3	13.5	9.2		
Co6	0.02	313	323	315	308	6.0	0.1	17.4	17.3	-2.6	
	5.0	300	316	306	294	6.0	6.0	91.7	85.7		
Co11	0.02	316	328	301	289	27	0.9	27.9	27.0	-6.6	
	5.0	283	301	263	244	38.5	13.0	109.1	96.1		

Table 2. Martensite transformation temperatures and magnetic properties obtained by vibrating sample magnetometer (VSM) for $Ni_{47-x}Mn_{43}Sn_{10}Co_x$ ($x = 0, 6, 11$) alloys under magnetic fields of 0.02 and 5.0 T. M_A and M_M are magnetizations of the austenite and martensite, respectively. ^{1*} $\Delta T_{Hys} = [(A_f + A_s) - (M_s + M_p)]/2$. ^{2*} Data obtained during heating process. ^{3*} $\Delta M = M_A - M_M$.

temperatures shift little to lower temperatures with increasing magnetic field ($\Delta A_s/\Delta H = -0.2$ K/T, as shown in Table 2 based on Fig. 3a), which is unfavorable to MCE². In contrast, both Co6 and Co11 alloys undergo the transformation between a weak-magnetic martensite and a ferromagnetic austenite (Fig. 3b,c), leading to higher ΔM .

Table 2 collected the MT and magnetic transition temperatures of the $Ni_{47-x}Mn_{43}Sn_{10}Co_x$ ($x = 0, 6, 11$) alloys. It can be seen that the MT temperatures determined from vibrating sample magnetometer (VSM) under 0.02 T are consistent with those from DSC (Table 1). The thermal hysteresis values ΔT_{Hys} , defined as $[(A_f + A_s) - (M_s + M_p)]/2$, are 6.0 K under both 0.02 and 5.0 T in the Co6 alloy, which are much smaller than those of 27 K (0.02 T) and 38.5 K (5.0 T) in the Co11 alloy. As the phase boundary friction strength during MT is responsible for ΔT_{Hys} ⁴⁸, this implies that the friction resistance during MT in Co11 alloy is larger than that in Co6 alloy.

It can also be seen from Table 2 that, during heating, the magnetization of the martensite M_M changes little but that of the austenite M_A increases significantly with increasing Co content. As a result, ΔM in Co6 and Co11 alloys reaches 85.7 and 96.1 A·m²/kg under a magnetic field 5.0 T, respectively, which is much higher than $\Delta M = 9.2$ A·m²/kg in Co0. The enhancement of ΔM favors the magnetic entropy change ΔS_M according to the Maxwell equation and broadens the ΔT_{FWHM} due to the increase in Zeeman energy⁴⁵. Furthermore, the percentage of MT caused by field-induced metamagnetic transition mainly relies on dT_M/dH ⁴⁰ (T_M denotes the MT equilibrium temperature, as shown in Fig. 3, which can be assessed by the Clausius-Clapeyron magnetic equation $-dT_M/dH = \Delta M/\Delta S_r$). Utilizing the values of ΔM under 5.0 T (Table 2) and ΔS_r determined by DSC (Table 1), the calculated $\Delta M/\Delta S_r$ is -2.5 and -5.4 K/T for Co6 and Co11, respectively. By contrast, the

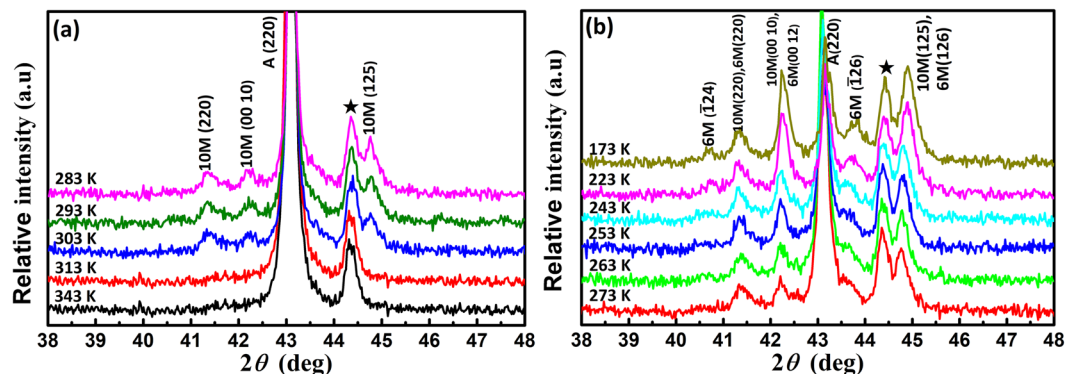


Figure 4. *In-situ* X-ray diffraction (XRD) patterns for Co6 alloy in the range $35^\circ < 2\theta < 50^\circ$ during cooling (a) from 343 K to 283 K and (b) from 273 K to 173 K, respectively. The diffraction peaks marked by five-pointed star corresponds to the sample stage.

magnetic-field-induced shift of the reverse MT temperature $\Delta A_s/\Delta H$ is -2.6 and -6.6 K/T for Co6 and Co11 alloys, respectively, as listed in Table 2. So, the applied 5.0 T magnetic field may induce a full metamagnetic transition from weak-magnetic martensite to ferromagnetic austenite in Co6 alloy, but only a partial transition in Co11 alloy, meaning that a 5.0 T magnetic field cannot compensate for the thermal energy loss during MT in Co11 alloy⁴⁸. Supposing a negligible difference of heat capacity between martensite/austenite phases, a maximum magnetic entropy change $\Delta S_M^{max} \approx \Delta S_H$ should be expected under a high $\Delta A_s/\Delta H$ ⁴⁹. As a result, a sizable inverse MCE in Co6 alloy is expected when taking the ΔM , ΔS_H , $\Delta A_s/\Delta H$ and ΔT_{Hys} into account.

In order to investigate the martensite transformation behavior of the Co6 alloy, X-Ray diffraction (XRD) measurements were performed in the temperature range 343–173 K during cooling process. The data were recorded at a temperature interval 10 K (except for 223 K and 173 K), as shown in Fig. 4. The diffraction peaks marked with five-pointed star are associated with the sample platform (Fig. 4). The martensite peaks were indexed as 10 M and 6 M martensite phases according to the theoretical calculation results⁵⁰ and is displayed in the Supplementary Materials Fig. S2. The alloy exhibits a $L2_1$ -type austenite structure at high temperatures. With decreasing temperature from 343 to 283 K, the peaks corresponding to the 10 M martensite occur starting at 303 K, as shown in Fig. 4a. As the temperature further decreases, several peaks associated with the 6 M martensite appear at 273 K (much lower than $M_f = 304$ K from Table 1), as shown in Fig. 4b. It can also be seen that the peak intensity of 6 M martensite becomes stronger with decreasing temperature. On the other hand, the peak intensity of 10 M martensite still keeps increasing with decreasing temperature after the occurrence of the 6 M martensite, implying the co-existence of the A, as shown 6 M transitions and the mixed A + 10 M + 6 M phase state during the MT process of the Co6 alloy. Such mixed state of 10 M and 6 M martensite phases has also been found in $Ni_{43}Co_7Mn_{39}Sn_{11}$ ⁵¹ and $Ni_{37}Co_{11}Mn_{43}Sn_9$ ⁵⁰ alloys. It is worth noting that the peak (220)_A of the $L2_1$ -type austenite can still be observed at temperature as low as 173 K (see Fig. 4b), indicating that an incomplete MT with residual austenite even at 173 K. This phenomenon is consistent with some other Ni-Mn-based alloys^{52,53}, implying that the complete MT might be difficult to be achieved supposing that slightly inhomogeneous composition distribution exists in the bulk alloy. Furthermore, the two successive magnetostructural transition processes (A \rightarrow 10 M and A \rightarrow 10 M + 6 M) in the present alloy are essentially different from the two successive martensite (MT) and intermartensite transition (IMT) occur in some other types of FMSMAs such as $Ni_{55.8}Mn_{18.1}Ga_{26.1}$ ⁴⁰, $Ni_{50}Mn_{13}In_{12}Sb_4$ ⁵⁴ and $Ni_{49-x}Cu_xMn_{38}Sn_{13}$ ($0.5 < x < 2$)⁵⁵ alloys.

In addition, the XRD pattern measured at 343 K ($A_f = 326$ K) is shown in Supplementary Materials Fig. S1b. Single austenite phase is detected without any secondary phases, which is consistent with the back scattered electron (BSE) micrograph observations (Supplementary Materials Fig. S1a). The result is consistent with that in $Ni_{34}Co_8Mn_{50}Sn_8$ ⁵⁶ and $Ni_{37}Co_{11}Mn_{43}Sn_9$ ⁵⁰ after annealing. Secondary phases were observed in $Ni_{42}Co_8Mn_{39}Sn_{11}$ ⁵⁷ and $Ni_{43}Co_7Mn_{39}Sn_{11}$ ⁵⁸ after annealing at 1173 K, however, the excessive Mn content in the present annealed Ni-Mn-Sn-Co alloys may have delayed the occurrence of secondary phase.

Magnetic properties of the $Ni_{40.6}Mn_{43.3}Sn_{10.0}Co_{6.1}$ (Co6) alloy. The temperature dependent FH/FC magnetization curves and the dM/dT vs T of the Co6 alloy recorded at magnetic fields 0.02, 1.0, 3.0 and 5.0 T are shown in Fig. 5a,b. It can be observed from Fig. 5a that slope changes in the FH/FC curves exist around MT temperatures at magnetic fields above 1.0 T. To clarify this phase transformation character, the first-derivative of the FC magnetization curves with respect to temperature ($dM/dT - T$) was plotted in Fig. 5b. Upon cooling, two successive maxima occur under magnetic fields of 1.0, 3.0 and 5.0 T, while only one inflection peak emerges at 0.02 T. Additionally, the $dM/dT - T$ curves show that M_s^{10M} and M_s^{6M} , denote as the 10 M and 6 M transformation starting temperatures, respectively, decrease with increasing magnetic field (i.e. the 10 M and 6 M change from 321 and 315 K under $\mu_0H = 1.0$ T to 308 and 301 K under $\mu_0H = 5.0$ T, respectively). This phenomenon probably indicate that the two successive magnetostructural transformations (A \rightarrow 10 M + 6 M and A \rightarrow 10 M) can be induced by an external magnetic field, which is still an open question and will be studied in the near future. Compared to the XRD patterns during cooling from 343 to 173 K (see Fig. 4), the magnetic-field-induced inverse martensite transformation is much easier than the temperature-field-induced one.

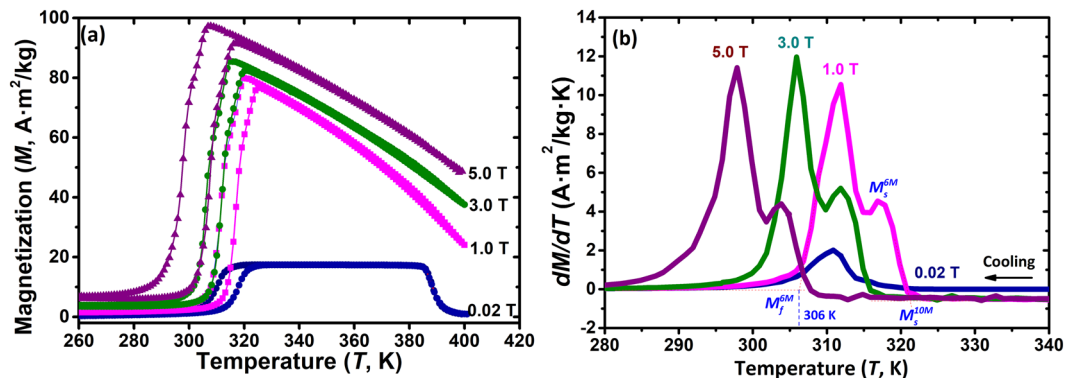


Figure 5. Magnetization curves as a function of temperature under magnetic fields of 0.02, 1.0, 3.0 and 5.0 T in the Co6 alloy. (a) Isofield magnetization (M - T) curves, (b) First-derivative plots of M - T .

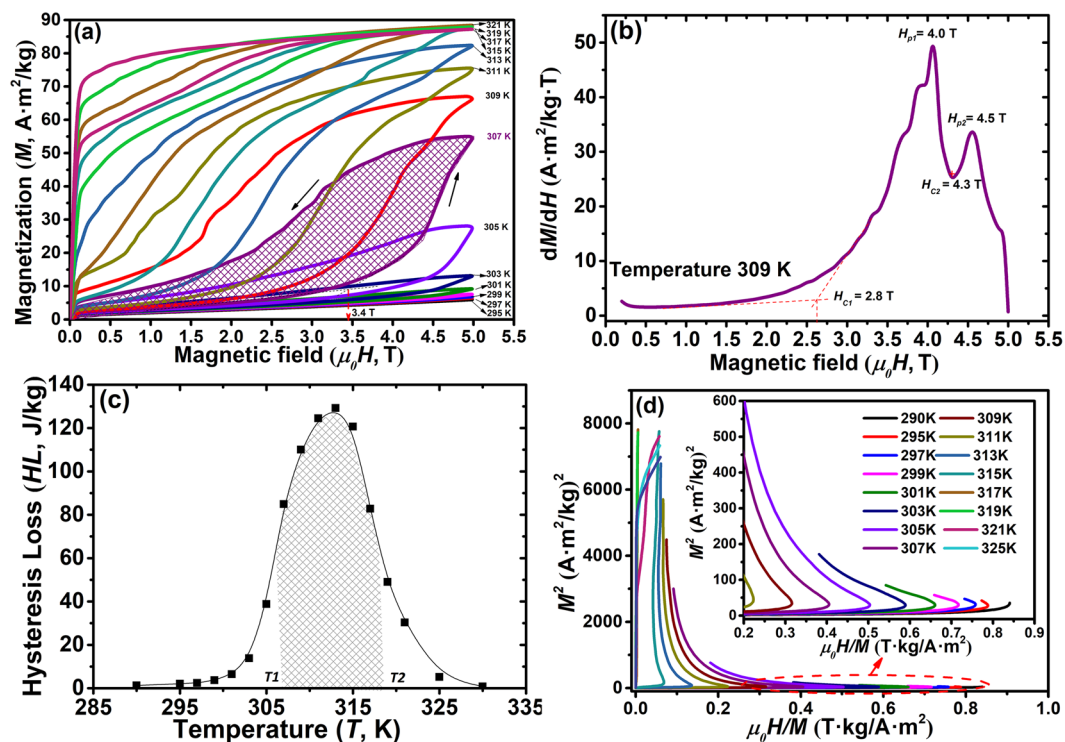


Figure 6. Magnetic transition behavior of the Co6 alloy. (a) Representative isothermal magnetization M - H loops under magnetic fields up to 5.0 T. (b) dM/dH curve measured at a temperature of 309 K showing two inflection points that indicate the occurrence of two successive magnetostructural transformations. (c) The temperature dependent hysteresis loss (HL) plot during the isothermal magnetization M - H cycling. The fitting line just acts as a guide for the eye. (d) Arrott (M^2 vs H/M) plots revealing the appearance of the magnetic-field-induced austenite (MIA) at temperatures above 295 K.

The isothermal magnetization M - H loops for Co6 alloy at temperatures 290–330 K are shown in Fig. 6a. The plots were recorded under magnetic field up to 5.0 T and at a temperature interval $\Delta T = 2$ K covering the A_s and A_f . At a temperature of 295 K, far below A_s^{VSM} (314 K in Table 1), no austenite was induced by magnetic field up to 5.0 T. When test temperatures approach A_s , the magnetic-field-induced austenite (MIA) transformation gradually occurs, with MIA critical magnetic field decreasing with increasing temperatures. At 307 K, a large jump in magnetization at about 3.4 T (Fig. 6a), due to the occurrence of MIA, was observed. After removing the magnetic field, the sample transformed back to martensite, but with a small amount of field-induced austenite remaining because the test temperature 307 K was slightly higher than M_f^{DSC} (304 K in Table 1)⁵⁹. The dM/dH curve measured at 309 K shows two successive inflection peaks centered at 4.0 and 4.5 T (as shown in Fig. 6b), implying the appearance of the two successive magnetostructural transformations. The first inflection peak at $H_{p1} = 4.0$ T corresponds to the field-induced inverse martensite transformation $6M + 10M \rightarrow A$, and the second

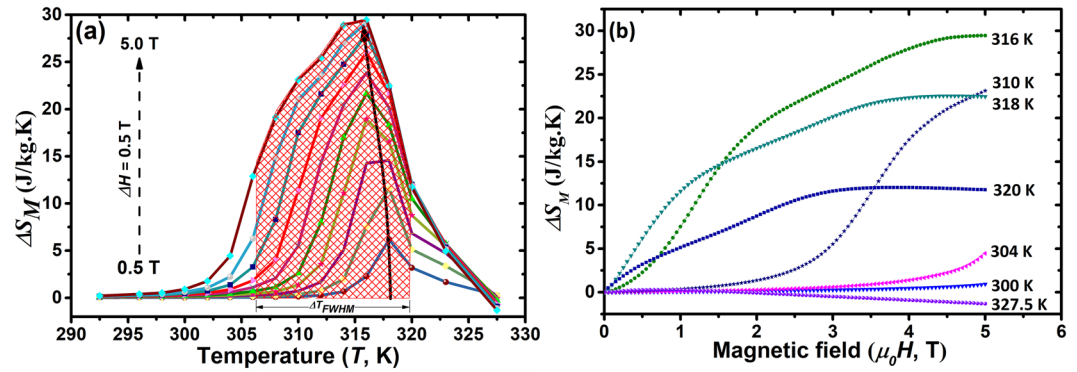


Figure 7. Magnetocaloric effects (MCE) of the Co6 alloy. (a) Selected temperature dependent magnetic entropy change (ΔS_M) curves under magnetic fields $\Delta H = 0.5$ – 5.0 T, (b) Magnetic entropy change ΔS_M as a function of the applied magnetic field at different temperatures in the reverse MT range.

peak at $H_{p2} = 4.5$ T to the $10\text{ M} \rightarrow \text{A}$. The fact that dM/dH under 4.0 T is larger than that under 4.5 T implies that the phase transition resistance of the former is smaller than the latter one.

During isothermal magnetization M - H cycling, the hysteresis loss (HL) was determined by integrating the areas between magnetization and demagnetization branches (purple shaded area in Fig. 6a). The temperature dependence of HL is plotted in Fig. 6c. The average hysteresis loss (AHL), calculated by averaging the integral area under the temperature range of the full width at half maximum of the hysteresis peak $AHL = \int_{T_1}^{T_2} \frac{f(HL)dT}{T_2 - T_1}$, (where $T_1 = 306$ K, $T_2 = 318$ K, as shown in Fig. 6c), was determined to be 99 J/kg under 5.0 T. This is comparable with those of the Ni-Mn-Sn-based alloys, i.e. $AHL = 138$ J/kg under 5.0 T in $\text{Ni}_{43}\text{Mn}_{46}\text{Sn}_{11}$ ¹⁷ and $AHL = 78$ J/kg under 3.0 T in $\text{Ni}_{45}\text{Co}_5\text{Mn}_{40}\text{In}_2\text{Sn}_8$ ⁶⁰ alloys. In order to reveal the first-order martensite transformation (FOMT) temperature, Arrott plots (M^2 vs $\mu_0 H/M$) were derived as shown in Fig. 6d. The negative slopes can be detected at temperatures ≥ 295 K, suggesting the occurrence of the magnetic-field-induced austenite (MIA) formation⁶¹. Furthermore, the large degree of negative slope indicates that MIA is fast¹⁸, which is consistent with the M - H curves displayed in Fig. 6a.

Magnetocaloric effects (MCE) of the $\text{Ni}_{40.6}\text{Mn}_{43.3}\text{Sn}_{10.0}\text{Co}_{6.1}$ (Co6) alloy. The MCE can be evaluated via ΔS_M calculated using thermodynamic Maxwell equation:

$$\Delta S_M(T, H) = S(T, H) - S(T, 0) = \int_0^H \frac{\partial M}{\partial T} dH.$$

Based on isothermal magnetization data with a field interval of $\Delta H_i = 0.05$ T at various temperatures (shown in Fig. 6a), the above partial derivative and integration may be numerically approximated to the equation:

$$\Delta S_M(T, H) = \sum_i \frac{M(T_{i+1}, H) - M(T_i, H)}{T_{i+1} - T_i} \Delta H_i.$$

The ΔS_M related to the FOMT for the Co6 alloy under $\Delta H = 0.5$ – 5.0 T is plotted as a function of temperature displayed in Fig. 7a. The positive ΔS_M is attributed to inverse MCE originating from a magnetic-field-induced metamagnetic transition from the weak-magnetic martensite to the ferromagnetic austenite phase². Additionally, the ΔS_M peak temperature exhibits a field-dependent behavior, i.e. shifting to lower temperatures with increasing magnetic fields.

As depicted in Fig. 6a, the magnetization saturates at lower fields with increasing temperature above A_s . According to the Maxwell equation, further increase of the magnetic field contributes little contribution to ΔS_M when the saturation magnetization plots intersect, such as the temperatures of 317 , 319 and 321 K in Fig. 6a. Therefore, the maximum ΔS_M (ΔS_M^{max}) for a field change 5.0 T can be achieved at a specific temperature, i.e. 314 K here in Co6 alloy, where the adjacent M - H curves at 313 and 315 K do not intersect. For the present Co6 alloy, the ΔS_M^{max} reaches 29.5 J/kg·K under a magnetic field 5.0 T, with a working temperature span ΔT_{FWHM} (defined as the full width at half maximum of ΔS_M^{max}) 306 – 320 K. The ΔS_M calculated from the Maxwell relation is compared with those from the Clausius-Clapeyron equation and DSC curves, as shown in Supplementary Materials TABLE S1. The ΔS_M^{max} is comparable to the value determined by Clausius-Clapeyron (32.9 J/kg·K), and both of them are also similar to the DSC results ($\Delta S_{\text{tr}}^{\text{endo}} = 33.7 \pm 0.2$ J/kg·K and $\Delta S_{\text{tr}}^{\text{exo}} = 32.2 \pm 0.2$ J/kg·K), implying that ΔS_M obtained by the Maxwell equation is acceptable in the present work without the occurrence of the so called ‘‘colossal’’ values around the transition temperature. In addition, the obtained ΔS_M^{max} in Co6 alloy is slightly higher than those of some other Co-doped Ni-Mn-based compounds whose ΔS_M^{max} were estimated using the loop-process method as well, such as $\text{Ni}_{50}\text{Co}_2\text{Mn}_{33}\text{In}_{15}$ (21.5 J/kg·K)⁶², $\text{Ni}_{45}\text{Co}_5\text{Mn}_{37.5}\text{In}_{12.5}$ (20 J/kg·K)⁶³, $\text{Ni}_{44}\text{Nb}_1\text{Co}_5\text{Mn}_{40}\text{Sn}_{10}$ (23 J/kg·K)⁶⁴ and $\text{Ni}_{40}\text{Co}_{10}\text{Mn}_{40}\text{Sn}_{10}$ (27 J/kg·K)¹³. Furthermore, the present ΔS_M^{max} is also comparable to some rare-earth containing magnetic refrigerants such as $\text{Gd}_5\text{Ge}_{2.3}\text{Si}_{1.7}$ (35.1 J/kg·K)⁶⁵, $\text{MnAs}_{0.97}\text{P}_{0.03}$ (33.4 J/kg·K)⁶⁶ and $\text{MnFeP}_{0.8}\text{Ge}_{0.2}$ (34.3 J/kg·K)⁶⁷.

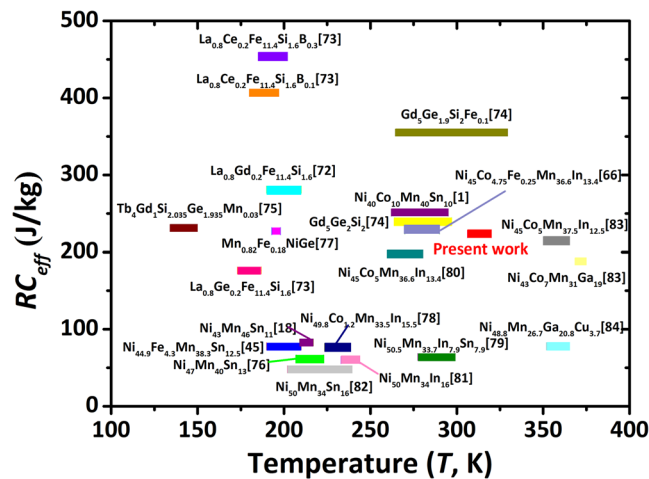


Figure 8. Effective magnetic refrigeration capacity RC_{eff} and working temperature span under a magnetic field of 5.0 T for the present Co6 alloy and some most studied magnetocaloric materials, such as La(FeSi) $_{13}$ -based^{72,73}, Gd $_5$ (SiGe) $_4$ -based^{74,75}, NiMn-based^{1,18,45,63,76–84} compounds. These alloys were selected because their magnetocaloric effects (MCE) are all related to the first-order martensite transformation and are tested around the magnetostructural transition temperatures.

On the other hand, MCE related to FOMT usually occurs in a narrow temperature range, for instance 1–5 K. By contrast, a broadened $\Delta T_{FWHM} \sim 14$ K was obtained in the present Co6 alloy, which may be attributed to two aspects: 1) Two successive magnetostructural transformations ($A \rightarrow 10$ M and $A \rightarrow 10$ M + 6 M), 2) Magnetic-field-induced metamagnetic transition, i.e. the magnetic field dependence of the ΔS_M^{max} position. Here, $A_f^{5.0T} > A_s^{0.02T}$ implies an incomplete reverse MT induced by a magnetic field of 5.0 T. In other words, the field-induced shift of the MT temperature cannot overcome MT width so that ΔS_M^{max} fails to saturate to ΔS_{Ir} . Whether a maximum of ΔS_M^{max} is reached under a field of 5.0 T needs further investigation in the near future. In Ni $_{45}$ Mn $_{36.7}$ In $_{13.3}$ Co $_5$ alloy, a maximum $\Delta S_M^{max} = 7$ J/kg K was achieved at a field of 4.0 T using “rectilinear modelization” by Recarte *et al.*⁶⁸. While ΔS_M^{max} of the Ni $_{45.5}$ Co $_{4.5}$ Mn $_{37}$ In $_{13}$ single crystal does not saturate up to 7.0 T using “curved modelization” adopted by Bourgault *et al.*⁶⁹. Both approaches are equally consistent with the experimental data at a low magnetic field range (<4.0 T), whereas the “curved modelization” is better in reflecting ΔS_M^{max} at high fields. The MCE tends to reach a saturation value for fields above 5.0 T in Ni $_5$ Mn $_{33.4}$ In $_{15.6}$ alloy by quasi-directly from isofield calorimetric measurements according to Stern *et al.*⁷⁰ Fig. 7b shows $\Delta S_M - T$ plots at different temperatures in the reverse MT range. At low temperatures (i.e. $T < 316$ K), the field-induced fraction of austenite phase increases with the rise of temperature, which is responsible to a similar increase in ΔS_M . At higher temperatures, where both martensite and austenite phases coexist at zero field, the field-induced austenite fraction and ΔS_M minify as the temperature increases. Furthermore, the negative slope of ΔS_M which can be clearly seen in Fig. 7b for high magnetic fields at 320 and 327.5 K, which is due to the contribution of this conventional direct MCE in the vicinity of T_C^A .

The refrigeration capacity (RC), which represents the amount of heat transferring between the cold and hot reservoirs in a thermodynamic cycle, is defined as $RC = \int_{T_{cold}}^{T_{hot}} |\Delta S_m(T)| dT$, where T_{cold} and T_{hot} are the corresponding temperatures at ΔT_{FWHM} of ΔS_M^{max} . By numerically integrating the area under the $\Delta S_M - T$ curves between T_{cold} and T_{hot} (shaded area in Fig. 7a), the $RC = 322$ J/kg under a magnetic field change of 5.0 T was obtained in Co6 alloy. However, for evaluating the effective magnetic refrigeration capacity, the AHL should be deducted^{18,45,71}. Therefore, a more reasonable criterion for assessing the cooling efficiency, the effective refrigeration capacity (RC_{eff}) defined as $RC_{eff} = RC - AHL$, was adopted here. For comparison, the RC_{eff} values under a field of 5.0 T for the present work and some most studied magnetocaloric materials^{1,18,45,63,72–84} are summarized in Fig. 8. Noteworthy, the RC_{eff} of the present Co6 alloy reaches 223 J/kg, which is significantly larger than those of the stoichiometric Ni-Mn-based alloys^{18,45,76,77,79,81–84} and is comparable to those of some Co-doped Mn-rich Ni-Mn-based compounds^{1,63,78–80,83}. Besides, the achieved RC_{eff} is also comparable to those rare-earth containing La(FeSi) $_{13}$ -based^{72,73} and Gd $_5$ (SiGe) $_4$ -based^{74,75} compounds. Of note is that the working temperature of the present alloy is slightly above 300 K, which is very encouraging for room-temperature magnetic refrigeration applications.

Conclusion

The effect of Co doping on the martensite transformation, magnetic properties and magnetocaloric effects were investigated in Ni $_{47-x}$ Mn $_{43}$ Sn $_{10}$ Co $_x$ ($x = 0, 6, 11$) alloys. The main conclusions may be drawn as follows:

- 1) The martensite transformation temperatures decreased and Curie temperature of austenite phase increased significantly with increasing Co concentration, broadening the temperature window for a higher magnetization of austenite: 13.5, 91.7 and 109.1 A·m 2 /kg for $x = 0, 6$ and 11, respectively.

- 2) Two successive magnetostructural transformations, i.e. $A \rightarrow 10M$ and $A \rightarrow 10M + 6M$, existed in the $\text{Ni}_{40.6}\text{Mn}_{43.3}\text{Sn}_{10.0}\text{Co}_{6.1}$ alloy whose magnetic-field-induced shift of austenite finishing temperature $\Delta A_f/\Delta H$ reached -2.6K/T .
- 3) A sizable maximum magnetic entropy change $\Delta S_M^{\text{max}} 29.5\text{J/kg}\cdot\text{K}$, a wide working temperature span $\Delta T_{\text{FWHM}} 14\text{K}$ and a high effective refrigeration capacity $RC_{\text{eff}} 223\text{J/kg}$ were obtained in the $\text{Ni}_{41}\text{Mn}_{43}\text{Sn}_{10}\text{Co}_6$ alloy under a magnetic field of 5.0T .

Methods

Sample and heat treatment. $\text{Ni}_{47-x}\text{Mn}_{43}\text{Sn}_{10}\text{Co}_x$ ($x = 0, 6, 11$, atomic percent) ingots, denoted as Co0, Co6 and Co11, respectively, were prepared by induction melting pure Ni (99.99%), Co (99.99%), Mn (99.9%) and Sn (99.99%) in an argon atmosphere and casting in a copper mold. The ingots were sealed in a quartz tube accompanied with Mn powder (to create a Mn vapor atmosphere in the tube) and Ti sheet (acted as oxygen getter), evacuated under vacuum at 10^{-2}Pa , annealed at 1173K for 24h and then quenched in iced-water. The composition of the specimens were determined by a Zeiss-SUPRA SEM equipped with an Oxford EDS, using 20kV voltage, $97\mu\text{A}$ emission current, 10mm working distance, $50\mu\text{A}$ probe current and $>60\text{s}$ data acquisition time duration. The composition measurement precision of the EDS was calibrated with chemical analysis results (ICP-OES) to be less than 0.5% .

Composition and martensite transformation tests. The actual and nominal compositions of the alloys were shown in Table 1. The microstructure of the specimens was examined by a Zeiss-SUPRA SEM and an Olympus PMG3 optical microscope (OM) with a polarizing filter. The martensite transformation temperatures and Curie points were measured by differential scanning calorimetry (DSC) at heating and cooling rates of $10\text{K}/\text{min}$. XRD analyses were performed using $\text{Cu K}\alpha$ radiation with a low-temperature chamber.

Magnetic property and magnetocaloric effects (MCE) evaluation. Magnetization measurements were performed using a vibrating sample magnetometer (VSM) in a commercial Magnetic Property Measurement System (MPMS) of Quantum Design. Magnetization vs temperature (M - T) curves were recorded under magnetic fields 0.02 and 5.0T with heating/cooling rates of $5\text{K}/\text{min}$ and temperature range 200 – 400K . Isothermal magnetization (M - H) curves were measured at different test temperatures (T_{test}) from temperatures 290 – 330K under an external magnetic field up to 5.0T . In order to rule out the temperature and field history effects and thus avoid the spurious spike, the so-called loop process⁸² was performed before each M - H test. The detailed loop process was as follows: 1) The sample was initially zero-field-cooled down to 200K to ensure a full weak-magnetic martensite state prior to recording each M - H cycle at a constant temperature, 2) Zero-field-heated to $(T_{\text{test}} - 10)\text{K}$ at $10\text{K}/\text{min}$, then heated to T_{test} at $1\text{K}/\text{min}$ and finally maintained at the T_{test} temperature for 2min before starting the M - H cycle.

Data availability statement. The datasets generated during and/or analyzed during the current study are available from the corresponding author on reasonable request.

References

1. Huang, L., Cong, D. Y., Suo, H. L. & Wang, Y. D. Giant magnetic refrigeration capacity near room temperature in $\text{Ni}_{40}\text{Co}_{10}\text{Mn}_{40}\text{Sn}_{10}$ multifunctional alloy. *Appl. Phys. Lett.* **104**, 132407 (2014).
2. Liu, J., Gottschall, T., Skokov, K. P., Moore, J. D. & Gutfleisch, O. Giant magnetocaloric effect driven by structural transitions. *Nature Mater.* **11**, 620–626 (2012).
3. L'Vov, V. A., Kosogor, A., Barandiaran, J. M. & Chernenko, V. A. Theoretical description of magnetocaloric effect in the shape memory alloy exhibiting metamagnetic behavior. *J. Appl. Phys.* **119**, 013902 (2016).
4. Chen, J. H., et al. Direct measure of giant magnetocaloric entropy contributions in Ni-Mn-In. *Acta Mater.* **105**, (2016).
5. Krautz, M. et al. Systematic investigation of Mn substituted $\text{La}(\text{Fe},\text{Si})_{13}$ alloys and their hydrides for room-temperature magnetocaloric application. *J. Alloy. Compd.* **598**, 27–32 (2014).
6. Sarkar, S. K. et al. Giant magnetocaloric effect from reverse martensitic transformation in Ni-Mn-Ga-Cu ferromagnetic shape memory alloys. *J. Alloy. Compd.* **670**, 281–288 (2016).
7. Deng, J. Q., Zhuang, Y. H., Li, J. Q. & Zhou, K. W. Magnetic phase transition and magnetocaloric effect in $(\text{Gd}_{1-x}\text{Tb}_x)_5\text{Si}_{1.72}\text{Ge}_{2.28}$ compounds. *J. Alloy. Compd.* **428**, 28–33 (2007).
8. Hu, F. X., Shen, B.-G. & Sun, J.-R. Magnetic entropy change involving martensitic transition in NiMn-based Heusler alloys. *Chin. Phys. B.* **22**, 037505 (2013).
9. Dubenko, I. et al. Magnetocaloric effect and multifunctional properties of Ni-Mn-based Heusler alloys. *J. Magn. Magn. Mater.* **324**, 3530–3534 (2012).
10. Quetz, A. et al. Giant reversible inverse magnetocaloric effects in $\text{Ni}_{50}\text{Mn}_{35}\text{In}_{15}$ Heusler alloys. *J. Alloy. Compd.* **683**, 139–142 (2016).
11. Dan, N. H. et al. Magnetic properties and magnetocaloric effect in Ni-Mn-Sn alloys. *J. Magn. Magn. Mater.* **374**, 372–375 (2015).
12. Umetsu, R. Y. et al. Metamagnetic behaviour under high magnetic fields in $\text{Ni}_{50}\text{Mn}_{50-x}\text{In}_x$ ($x = 14.0$ and 15.6) shape memory alloys. *J. Phys. D: Appl. Phys.* **42**, 075003 (2009).
13. Wang, X. et al. Influence of annealing temperatures on the magnetostructural transition and magnetocaloric effect of $\text{Ni}_{40}\text{Co}_{10}\text{Mn}_{40}\text{Sn}_{10}$ powders. *J. Alloy. Compd.* **691**, 215–219 (2017).
14. Pandey, S. et al. Effects of annealing on the magnetic properties and magnetocaloric effects of B doped Ni-Mn-In melt-spun ribbons. *J. Alloy. Compd.* **731**, 678–684 (2018).
15. Liu, J., Scheerbaum, N., Lyubina, J. & Gutfleisch, O. Reversibility of magnetostructural transition and associated magnetocaloric effect in Ni-Mn-In-Co. *Appl. Phys. Lett.* **93**, 102512 (2008).
16. Zhang, Y. et al. Large magnetic entropy change and enhanced mechanical properties of Ni-Mn-Sn-C alloys. *Scripta Mater.* **75**, 26–29 (2014).
17. Şaşıoğlu, E., Sandratskii, L. M. & Bruno, P. First-principles calculation of the intersublattice exchange interactions and Curie temperatures of the full Heusler alloys Ni_2MnX ($X = \text{Ga}, \text{In}, \text{Sn}, \text{Sb}$). *Phys. Rev. B.* **70**, 024427 (2004).
18. Zhang, Y. et al. Enhanced large magnetic entropy change and adiabatic temperature change of $\text{Ni}_{43}\text{Mn}_{46}\text{Sn}_{11}$ alloys by a rapid solidification method. *Scripta Mater.* **104**, 41–44 (2015).
19. Das, R., Sarma, S., Perumal, A. & Srinivasan, A. Effect of Co and Cu substitution on the magnetic entropy change in $\text{Ni}_{46}\text{Mn}_{43}\text{Sn}_{11}$ alloy. *J. Appl. Phys.* **109**, 07A901 (2011).

20. Bruno, N. M. *et al.* Effect of grain constraint on the field requirements for magnetocaloric effect in Ni₄₅Co₅Mn₄₀Sn₁₀ melt-spun ribbons. *J. Appl. Phys.* **120**, 075101 (2016).
21. Bruno, N. M. *et al.* The effect of heat treatments on Ni₄₃Mn₄₂Co₄Sn₁₁ meta-magnetic shape memory alloys for magnetic refrigeration. *Acta Mater.* **74**, 66–84 (2014).
22. Qu, Y. H. *et al.* Giant and reversible room-temperature magnetocaloric effect in Ti-doped Ni-Co-Mn-Sn magnetic shape memory alloys. *Acta Mater.* **134**, 236–248 (2017).
23. Cong, D. Y. *et al.* Low-field-actuated giant magnetocaloric effect and excellent mechanical properties in a NiMn-based multiferroic alloy. *Acta Mater.* **146**, 142–151 (2018).
24. Liu, C. *et al.* Martensitic transition, inverse magnetocaloric effect and shape memory characteristics in Mn_{48-x}Cu_xNi₄₂Sn₁₀ Heusler alloys. *Phys. Rev. B: Condens. Matter.* **508**, 118–123 (2017).
25. Tan, C., Tai, Z., Zhang, K., Tian, X. & Cai, W. Simultaneous enhancement of magnetic and mechanical properties in Ni-Mn-Sn alloy by Fe doping. *Sci. Rep.* **7**, 43387 (2017).
26. Tan, C. L. *et al.* Microstructure, martensitic transformation and mechanical properties of Ni-Mn-Sn alloys by substituting Fe for Ni. *Trans. Nonferrous Met. Soc. China.* **27**, 2234–2238 (2017).
27. Zhang, H. H. *et al.* Enhanced magnetocaloric effects of Ni-Fe-Mn-Sn alloys involving strong metamagnetic behavior. *J. Alloy. Compd.* **715**, 206–213 (2017).
28. Sharma, J. & Suresh, K. G. Investigation of multifunctional properties of Mn₅₀Ni_{40-x}Co_xSn₁₀ (x = 0–6) Heusler alloys. *J. Alloy. Compd.* **620**, 329–336 (2015).
29. Zheng, H., Wang, W., Yu, J., Zhai, Q. & Luo, Z. Martensitic transformation in melt-spun Heusler Ni-Mn-Sn-Co ribbons. *J. Mater. Res.* **29**, 880–886 (2014).
30. Cong, D. Y., Roth, S. & Schultz, L. Magnetic properties and structural transformations in Ni-Co-Mn-Sn multifunctional alloys. *Acta Mater.* **60**, 5335–5351 (2012).
31. Guo, Z. G., Pan, L. Q., Qiu, H. M., Zheng, X. F. & Liu, Z. H. Structural and magnetic phase transition in quinary Ni₄₅Co₅(Mn, In, Sn)₅₀ Heusler alloy. *J. Alloy. Compd.* **615**, 316–321 (2014).
32. Ito, W. *et al.* Martensitic and magnetic transformation behaviors in Heusler-type NiMnIn and NiCoMnIn metamagnetic shape memory alloys. *Metall. Mater. Trans. A.* **38**, 759–766 (2007).
33. Wu, Z. G., Liu, Z. H., Yang, H., Liu, Y. N. & Wu, G. H. Effect of Co addition on martensitic phase transformation and magnetic properties of Mn₅₀Ni_{40-x}In₁₀Co_x polycrystalline alloys. *Intermetallics.* **19**, 1839–1848 (2011).
34. Karaca, H. E. *et al.* Magnetic field-induced phase transformation in NiMnCoIn magnetic shape-memory alloys—A new actuation mechanism with large work output. *Adv. Funct. Mater.* **19**, 983–998 (2009).
35. Wu, Z. G. Development of Ni-Mn-Based Ferromagnetic Shape Memory Alloys. *The University of Western Australia. Ph.D. Thesis.* 20–21 (2011).
36. Li, G. X. *et al.* Successive magnetic phase transitions in TbMn₂Si₂ for magnetic refrigeration. *Appl. Phys. Lett.* **106**, 182405 (2015).
37. Chen, J., Shen, B. G., Dong, Q. Y., Hu, F. X. & Sun, J. R. Large reversible magnetocaloric effect caused by two successive magnetic transitions in ErGa compound. *Appl. Phys. Lett.* **95**, 132504 (2009).
38. Meng, H. *et al.* Reversible magnetocaloric effect and refrigeration capacity enhanced by two successive magnetic transitions in DyB₂. *Sci. China. Technol. Sc.* **55**, 501–504 (2012).
39. Li, L. W., Namiki, T., Huo, D. X., Qian, Z. H. & Nishimura, K. Two successive magnetic transitions induced large refrigerant capacity in HoPdIn compound. *Appl. Phys. Lett.* **103**, 222405 (2013).
40. Li, Z. *et al.* Two successive magneto-structural transformations and their relation to enhanced magnetocaloric effect for Ni_{55.8}Mn_{18.1}Ga_{26.1} Heusler alloy. *Sci. Rep.* **5**, 15143 (2015).
41. Ma, S. C. *et al.* Investigation of the intermediate phase and magnetocaloric properties in high-pressure annealing Ni-Mn-Co-Sn alloy. *Appl. Phys. Lett.* **97**, 052506 (2010).
42. Zhang, X. X. *et al.* Enhanced magnetic entropy change and working temperature interval in Ni-Mn-In-Co alloys. *J. Alloy. Compd.* **656**, 154–158 (2016).
43. Krenke, T. *et al.* Ferromagnetism in the austenitic and martensitic states of Ni-Mn-In alloys. *Phys. Rev. B.* **73**, 174413 (2006).
44. Krenke, T. *et al.* Martensitic transitions and the nature of ferromagnetism in the austenitic and martensitic states of Ni-Mn-Sn alloys. *Phys. Rev. B.* **72**, 014412 (2005).
45. Zhang, H. H. *et al.* Magnetocaloric effect of Ni-Mn-Sn-Fe microwires prepared by melt-extraction technique. *Mater. Des.* **114**, 1–9 (2017).
46. Mohd Jani, J., Leary, M., Subic, A. & Gibson, M. A. A review of shape memory alloy research, applications and opportunities. *Mater. Des.* **56**, 1078–1113 (2014).
47. Webster, P. J., Ziebeck, K. R. A., Town, S. L. & Peak, M. S. Magnetic order and phase transformation in Ni₂MnGa. *Philos. Mag. B.* **49**, 295–310 (1984).
48. Wang, W. H., Chen, J. L., Liu, Z. H., Wu, G. H. & Zhan, W. S. Thermal hysteresis and friction of phase boundary motion in ferromagnetic Ni₅₂Mn₂₃Ga₂₅ single crystals. *Phys. Rev. B.* **65**, 012416 (2002).
49. Pecharsky, V. K., Gschneider, K. A., Pecharsky, A. O. & Tishin, A. M. Thermodynamics of the magnetocaloric effect. *Phys. Rev. B.* **64**, 144406 (2001).
50. Umetsu, R. Y. *et al.* Kinetic arrest behavior in martensitic transformation of NiCoMnSn metamagnetic shape memory alloy. *J. Alloy. Compd.* **509**, 1389–1393 (2011).
51. Kainuma, R. *et al.* Metamagnetic shape memory effect in a Heusler-type Ni₄₅Co₇Mn₃₉Sn₁₁ polycrystalline alloy. *Appl. Phys. Lett.* **88**, 192513 (2006).
52. Liu, D. M. *et al.* In-situ studies of stress- and magnetic-field-induced phase transformation in a polymer-bonded Ni-Co-Mn-In composite. *Mater. Sci. Eng., A.* **527**, 3561–3571 (2010).
53. Chatterjee, S., Giri, S., Majumdar, S. & De, S. K. Thermomagnetic irreversibility in Ni₂Mn_{1.36}Sn_{0.64} shape-memory alloy. *Phys. Rev. B.* **77**, 224440 (2008).
54. Yu, S. Y. *et al.* Intermartensitic transformation and magnetic field effect in NiMnInSb ferromagnetic shape memory alloys. *J. Magn. Mater.* **322**, 2541–2544 (2010).
55. Esakki Muthu, S. *et al.* Influence of chemical substitution, magnetic field, and hydrostatic pressure effect on martensitic and intermartensitic transition in bulk Ni_{49-x}Cu_xMn₃₈Sn₁₃ (0.5 ≤ x ≤ 2) Heusler alloys. *Appl. Phys. Lett.* **104**, 092404 (2014).
56. Wu, Z., Liu, Z., Yang, H., Liu, Y. & Wu, G. Martensitic and magnetic transformation behaviours in Mn₅₀Ni_{42-x}Sn₈Co_x polycrystalline alloys. *J. Phys. D: Appl. Phys.* **44**, 385403 (2011).
57. Lázpita, P. *et al.* Martensitic transformation and magnetic field induced effects in Ni₄₂Co₈Mn₃₉Sn₁₁ metamagnetic shape memory alloy. *Acta Mater.* **109**, 170–176 (2016).
58. Pérez-Sierra, A. M., Pons, J., Santamarta, R., Vermaut, P. & Ochin, P. Solidification process and effect of thermal treatments on Ni-Co-Mn-Sn metamagnetic shape memory alloys. *Acta Mater.* **93**, 164–174 (2015).
59. Liu, J., Woodcock, T. G., Scheerbaum, N. & Gutfleisch, O. Influence of annealing on magnetic field-induced structural transformation and magnetocaloric effect in Ni-Mn-In-Co ribbons. *Acta Mater.* **57**, 4911–4920 (2009).
60. Guo, Z. G. *et al.* Metamagnetic phase transformation and magnetocaloric effect in quinary Ni₄₅Co₅Mn₄₀In_xSn_{10-x} heusler alloy. *J. Alloy. Compd.* **577**, 174–178 (2013).
61. Zhao, J. L. *et al.* Reduction of magnetic hysteresis loss in La_{0.5}Pr_{0.5}Fe_{11.4}Si_{1.6}H_x hydrides with large magnetocaloric effects. *J. Appl. Phys.* **107**, 113911 (2010).

62. Li, Z., Zhang, Y. L., Xu, K. & Jing, C. Large magnetocaloric effect related to martensitic transformation in $\text{Ni}_{50}\text{Co}_2\text{Mn}_{33}\text{In}_{15}$ textured alloy. *Phys. Rev. B: Condens. Matter.* **476**, 179–182 (2015).
63. Bourgault, D., Tillier, J., Courtois, P., Maillard, D. & Chaud, X. Large inverse magnetocaloric effect in $\text{Ni}_{45}\text{Co}_5\text{Mn}_{37.5}\text{In}_{12.5}$ single crystal above 300 K. *Appl. Phys. Lett.* **96**, 132501 (2010).
64. Emre, B., Bruno, N. M., Emre, S. Y. & Karaman, I. Effect of niobium addition on the martensitic transformation and magnetocaloric effect in low hysteresis NiCoMnSn magnetic shape memory alloys. *Appl. Phys. Lett.* **105**, 231910 (2014).
65. Caron, L. *et al.* On the determination of the magnetic entropy change in materials with first-order transitions. *J. Magn. Magn. Mater.* **321**, 3559–3566 (2009).
66. Sun, N. K. *et al.* Effect of microstrain on the magnetism and magnetocaloric properties of $\text{MnAs}_{0.97}\text{P}_{0.03}$. *Appl. Phys. Lett.* **100**, 112407 (2012).
67. Yibole, H., Guillou, F., Zhang, L., van Dijk, N. H. & Bruck, E. Direct measurement of the magnetocaloric effect in MnFe(P,X) (X = As, Ge, Si) materials. *J. Phys. D: Appl. Phys.* **47**, 075002 (2014).
68. Recarte, V., Perez-Landazabal, J. I., Kustov, S. & Cesari, E. Entropy change linked to the magnetic field induced martensitic transformation in a Ni-Mn-In-Co shape memory alloy. *J. Appl. Phys.* **107**, (2010).
69. Bourgault, D., Porcar, L., Rivoirard, S., Courtois, P. & Hardy, V. Entropy change of a $\text{Ni}_{45.5}\text{Co}_{4.5}\text{Mn}_{37}\text{In}_{13}$ single crystal studied by scanning calorimetry in high magnetic fields: Field dependence of the magnetocaloric effect. *Appl. Phys. Lett.* **107**, 092403 (2015).
70. Stern-Taulats, E. *et al.* Magnetocaloric effect in the low hysteresis Ni-Mn-In metamagnetic shape-memory Heusler alloy. *J. Appl. Phys.* **115**, 173907 (2014).
71. Ma, S. C. *et al.* Wheel speed-dependent martensitic transformation and magnetocaloric effect in Ni-Co-Mn-Sn ferromagnetic shape memory alloy ribbons. *Acta Mater.* **90**, 292–302 (2015).
72. Shamba, P., Zeng, R., Wang, J. L., Campbell, S. J. & Dou, S. X. Enhancement of the refrigerant capacity in low level boron doped $\text{La}_{0.8}\text{Gd}_{0.2}\text{Fe}_{11.4}\text{Si}_{1.6}$. *J. Magn. Magn. Mater.* **331**, 102–108 (2013).
73. Shamba, P. *et al.* Reduction of hysteresis losses in the magnetic refrigerant $\text{La}_{0.8}\text{Ce}_{0.2}\text{Fe}_{11.4}\text{Si}_{1.6}$ by the addition of boron. *J. Appl. Phys.* **109**, 07A940 (2011).
74. Provenzano, V., Shapiro, A. J. & Shull, R. D. Reduction of hysteresis losses in the magnetic refrigerant $\text{Gd}_5\text{Ge}_2\text{Si}_2$ by the addition of iron. *Nature.* **430**, 810–810 (2004).
75. Min, J. X. *et al.* Structure, magnetic properties and giant magnetocaloric effect of $\text{Tb}_4\text{Gd}_1\text{Si}_{2.03}\text{Ge}_{1.935}\text{Mn}_{0.03}$ alloy. *Intermetallics.* **57**, 68–72 (2015).
76. Varzaneh, A. G. *et al.* Effect of Cu substitution on magnetocaloric and critical behavior in $\text{Ni}_{47}\text{Mn}_{40}\text{Sn}_{13-x}\text{Cu}_x$ alloys. *J. Alloy. Compd.* **708**, 34–42 (2017).
77. Wu, R. *et al.* Critical dependence of magnetostructural coupling and magnetocaloric effect on particle size in Mn-Fe-Ni-Ge compounds. *Sci. Rep.* **6**, 20993 (2016).
78. Huang, L. *et al.* Large reversible magnetocaloric effect in a Ni-Co-Mn-In magnetic shape memory alloy. *Appl. Phys. Lett.* **108**, 032405 (2016).
79. Dwevedi, S. & Tiwari, B. Martensitic transformations and magnetocaloric effect in Sn-doped NiMnIn shape memory alloy. *J. Alloy. Compd.* **540**, 16–20 (2012).
80. Chen, L. *et al.* Magnetoresistance and magnetocaloric properties involving strong metamagnetic behavior in Fe-doped $\text{Ni}_{45}(\text{Co}_{1-x}\text{Fe}_x)_5\text{Mn}_{36}\text{In}_{13.4}$ alloys. *Appl. Phys. Lett.* **101**, 012401 (2012).
81. Chattopadhyay, M. K., Sharma, V. K. & Roy, S. B. Thermomagnetic history dependence of magnetocaloric effect in $\text{Ni}_{50}\text{Mn}_{34}\text{In}_{16}$. *Appl. Phys. Lett.* **92**, 022503 (2008).
82. Sharma, V. K. *et al.* Magnetocaloric effect in Heusler alloys $\text{Ni}_{50}\text{Mn}_{34}\text{In}_{16}$ and $\text{Ni}_{50}\text{Mn}_{34}\text{Sn}_{16}$. *J. Phys.: Condens. Matter.* **19**, 496207 (2007).
83. Fabbri, S. *et al.* From direct to inverse giant magnetocaloric effect in Co-doped NiMnGa multifunctional alloys. *Acta Mater.* **59**, 412–419 (2011).
84. Zhang, X. X. *et al.* Magnetostructural coupling and magnetocaloric effect in Ni-Mn-Ga-Cu microwires. *Appl. Phys. Lett.* **108**, 052401 (2016).

Acknowledgements

Financial supports from National Key R&D Program of China (grant number 2017YFB0703103), National Natural Science Foundation of China (NSFC) (grant number 51701052) and the Fundamental Research Funds for the Central Universities (grant number HIT.NSRIF.201801) are greatly acknowledged.

Author Contributions

X.X.Z proposed and led the project, analyzed the data and wrote the manuscript. H.H.Z observed the microstructure, carried out the martensite transformation and magnetocaloric effects tests, summarized the data and wrote the manuscript. M.F.Q analyzed the data and revised the manuscript. L.G supervised the project and revised the manuscript. All authors contributed to the discussions of the data and reviewed the manuscript.

Additional Information

Supplementary information accompanies this paper at <https://doi.org/10.1038/s41598-018-26564-5>.

Competing Interests: The authors declare no competing interests.

Publisher's note: Springer Nature remains neutral with regard to jurisdictional claims in published maps and institutional affiliations.



Open Access This article is licensed under a Creative Commons Attribution 4.0 International License, which permits use, sharing, adaptation, distribution and reproduction in any medium or format, as long as you give appropriate credit to the original author(s) and the source, provide a link to the Creative Commons license, and indicate if changes were made. The images or other third party material in this article are included in the article's Creative Commons license, unless indicated otherwise in a credit line to the material. If material is not included in the article's Creative Commons license and your intended use is not permitted by statutory regulation or exceeds the permitted use, you will need to obtain permission directly from the copyright holder. To view a copy of this license, visit <http://creativecommons.org/licenses/by/4.0/>.